Supplementary Information: Universal control of four singlet-triplet qubits

Xin Zhang,[1,2,*] Elizaveta Morozova,[1,2,*] Maximilian Rimbach-Russ,[1,2] Daniel Jirovec,[1,2] Tzu-Kan Hsiao,[1,2] Pablo Cova Fariña,[1,2] Chien-An Wang,[1,2] Stefan D. Oosterhout,[1,3] Amir Sammak,[1,3] Giordano Scappucci,[1,2] Menno Veldhorst,[1,2] and Lieven M. K. Vandersypen[1,2,†]

[1] *QuTech, Delft University of Technology, Delft, The Netherlands.*
[2] *Kavli Institute of Nanoscience, Delft University of Technology, Delft, The Netherlands.*
[3] *Netherlands Organisation for Applied Scientific Research (TNO), Delft, The Netherlands.*

(Dated: December 28, 2023)

This supplementary information includes:

I. EXPERIMENTAL SETUP

A schematic of the measurement setup is shown in Fig. 1. The device is thermally anchored to the mixing chamber of a dilution refrigerator with a base temperature of around 10 mK. All the control electronics are at room temperature, which connect the device via 50 direct current (DC) lines and 24 alternating current (AC) lines in total. The DC and AC signals are combined using bias tees on the printed circuit board (PCB) to apply both signals to the same gate of the device. DC signals are produced by custom-built battery-powered DC voltage sources and are fed through a matrix module—a breakout box with filters inside—to the Fisher cables of the fridge. AC signals are produced by 6 Keysight M3202A modules which are connected directly to the coaxial lines in the fridge. For the filters, we use common-mode Ferrite chokes at room temperature to filter low-frequency noise (10 kHz - 1 MHz) in the ground of AC lines and use RC filters as well as copper-powder filters that are mounted on the cold finger attached to the mixing chamber plate to filter high-frequency noise in DC lines.

The sensing dots are measured using radio-frequency (RF) reflectometry with working frequencies of 179 MHz, 190 MHz, 124 MHz and 158 MHz for sensor S_{TL}, S_{BL}, S_{TR} and S_{BR}, respectively. Tank circuits are formed by NbTiN inductors mounted on the PCB and the spurious capacitance of the bonding wires and metal lines on the board and chip. We apply RF signals using custom-built RF generators and combine them into a single coaxial line at room temperature using a power combiner ZFSC-3-1W-S+. The signal is attenuated at each plate in the dilution refrigerator and passes through a directional coupler (ZEDC-15-2B) at the mixing chamber to reach the device. The signal reflected from the device goes through the same directional coupler and is then amplified with a CITLF3 cryogenic amplifier at the 4K plate. At room temperature, the signal is amplified again and demodulated by custom-built IQ mixers. The demodulated signal is sent to the Keysight M3102A module to convert analog readout signals to digital signals. We use DC blocks to reduce low-frequency noise (< 10 MHz) in the RF lines. The DC block inside the refrigerator blocks the DC signal on the inner conductor (PE8210) while the ones at room temperature block that on both the inner and outer conductor (PE8212). To suppress high-frequency noise in the reflected signal, we use a low-pass filter (SBLP-300+) at room temperature.

* These authors contributed equally to this work
† L.M.K.Vandersypen@tudelft.nl

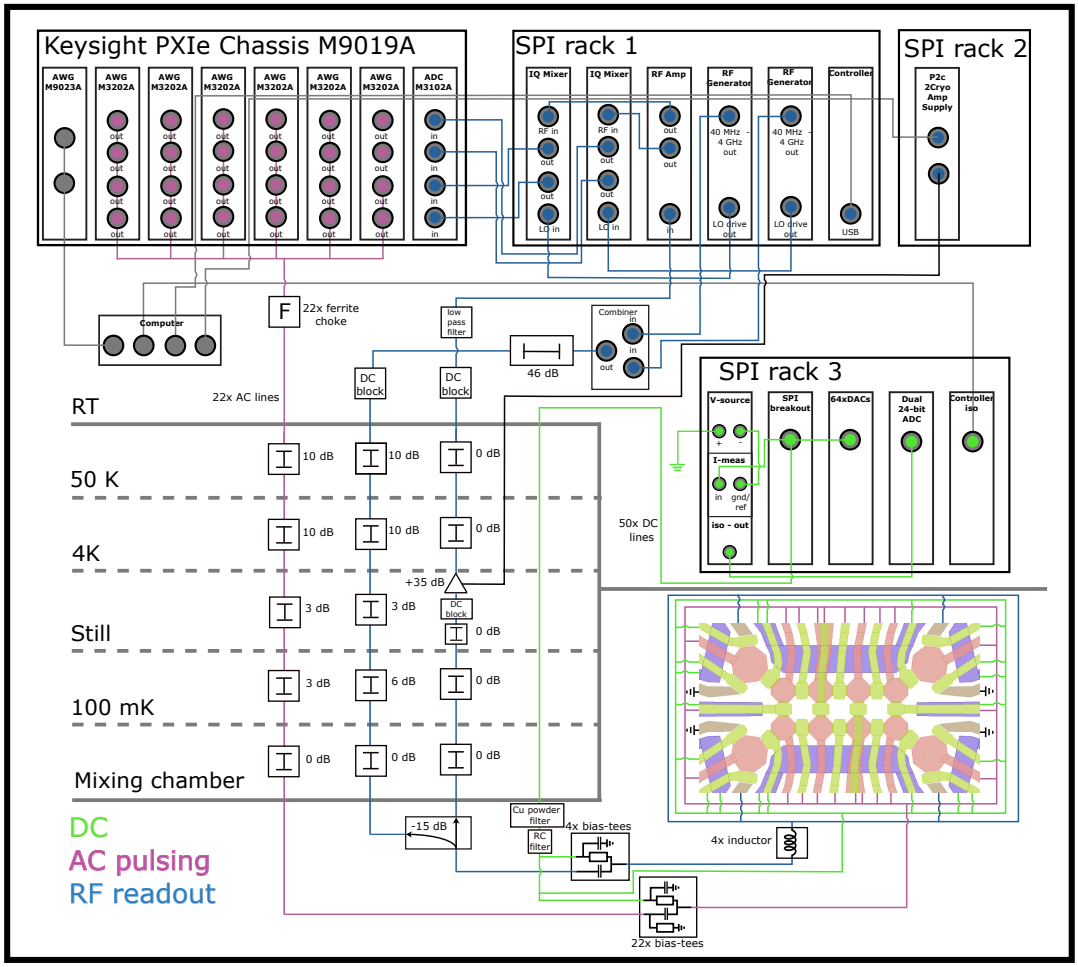

FIG. 1. Measurement circuit for the device. The DC and AC control lines as well as radio-frequency (RF) readout lines are fed from room-temperature instruments to the device at a base temperature of the dilution refrigerator through the cables and various electronic components shown in the figure. The room-temperature instruments include three custom-built SPI racks for supplying DC voltages and RF readout signals, and one Keysight PXIe Chassis for AC pulsing (arbitrary waveform generator, AWG) and data acquisition (analog-to-digital converter, ADC).

II. CHARGE STABILITY DIAGRAMS AND SPIN READOUT

Charge stability diagrams for DQD 1-5, 2-6, 3-7, and 4-8 are shown in Fig. 2a-d, respectively, where we tune all quantum dots to the single-hole regime. To measure the spin states of each DQD, we utilize Pauli-spin blockade (PSB) with diabatic pulses to the readout point [1]. For outer DQD 1-5 and 4-8, as shown by the stability diagram in Fig. 2a and d, we find PSB by pulsing ε_{15} and ε_{48} from (1,1) to (2,0) and (0,2), where within a triangular region an electron tunnels between the dots starting from the $S(1,1)$ but no tunneling occurs (the system is in Pauli spin blockade) from $T_0(1,1)$, $T_-(1,1)$ and $T_+(1,1)$.

As for DQD 2-6 and 3-7, we convert their spin states to those of DQD 5-6 and 7-8 where the sensor signals are stronger. In the following, we take pair 2-6 as an example to explain the readout process of the inner spin pairs. First, we align DQD 1-5 at the charge stability boundary between (2,0) and (2,1), as shown by the white dot in Fig. 2a, and then pulse ε_{26} from negative to positive. We subsequently find a shaded region between (0,1) and (0,2) in the diagram for DQD 2-6, which is caused by PSB in DQD 5-6. The mechanism is shown in Fig. 2e: when we pulse DQD 2-6 to the point where $S(0,2)$ is lower in energy than $(0,1)$, the holes in DQD 2-6 moves across to DQD 5-6, irrespective of the spin states. Subsequently, the conventional PSB mechanism in DQD 5-6 allows $S(1,1)$ to transition to $S(0,2)$, while the triplets $T(1,1)$ have to remain in the (1,1) charge state. In this way, we indirectly realize spin-to-charge conversion for the two spins initially in DQD 2-6. Actually, $S(1,1)$ in DQD 2-6 can also directly tunnel to $S(0,2)$ inside the same DQD, as seen by the curved arrow in Fig. 2e. The mechanism to measure DQD 3-7 is analogous.

In the experiment, we repeatedly perform single-shot readout cycles to obtain singlet or triplet probabilities. The

integration time for each single-shot readout is around 20-40 μs, depending on the signal-to-noise ratio during measurements. To compensate for the drift of the sensor signal, we use a reference readout segment before each measurement sequence [2]. For some datasets, we adjust the single-shot readout threshold by post-processing instead of through a reference segment. In post-processing, we collect a histogram for each data point that includes 1000-4000 shots based on which we set the threshold to analyze those shots. In this way, sensor drift between data points is mostly filtered out. The total measurement time needed to collect the data for each 2-dimensional plot in Fig. 1f-i, Fig. 2c-j, Fig. 3d-f and Fig. 4b-c is around 20-40 minutes, using 1000-2000 shots per data point. For the 1-dimensional plot in Fig. 2o and p, the measurement time of each trace is 10-50 minutes with 1000-4000 shots per data point, while for that in Fig. 3g, it is 2 minutes with 1000 shots per data point.

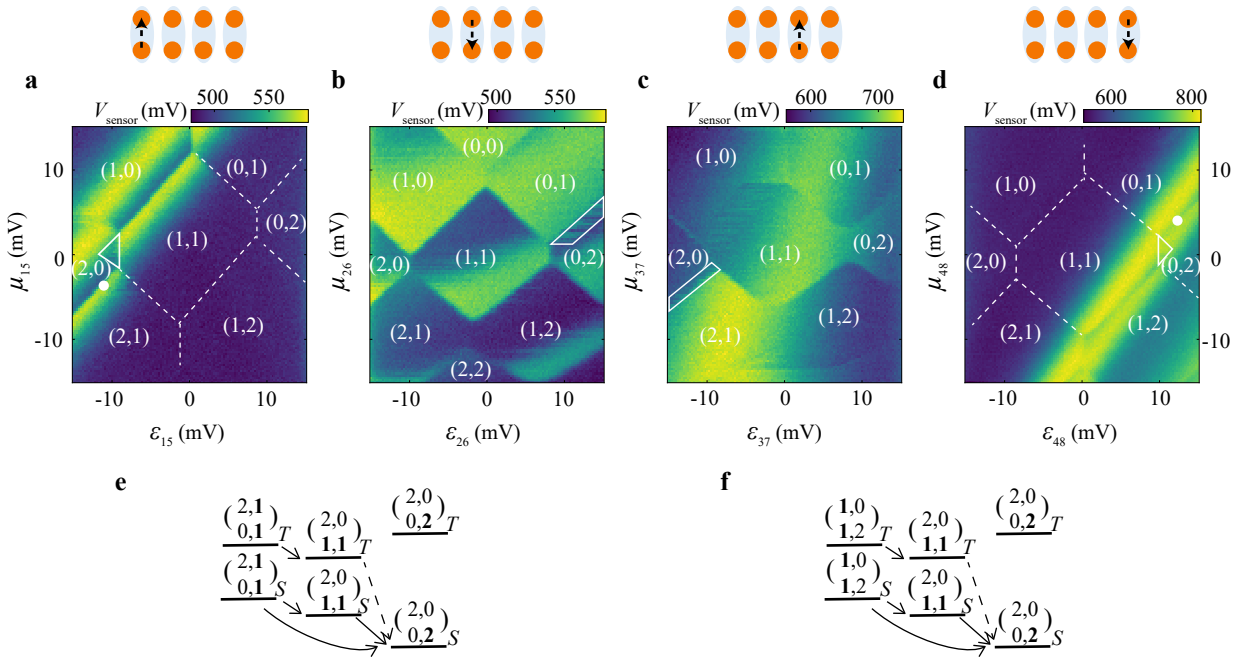

FIG. 2. **a-d**, Charge stability diagrams for DQD 1-5 (**a**), 2-6 (**b**), 3-7 (**c**), and 4-8 (**d**), respectively. **a** and **b** are recorded using the sensor S_{BL} while **c** and **d** are recorded using the sensor S_{BR}. The hole numbers inside the Coulomb blockade region are indicated. The PSB regions are shown by solid white triangles and trapezoids. **e**,**f**, Illustration of PSB using the energy levels in the quadruple quantum dot plaquette for DQD 2-6 (**e**) and 3-7 (**f**), respectively. The hole numbers are indicated as $\left(\begin{smallmatrix} n_1, & n_2 \\ n_5, & n_6 \end{smallmatrix}\right)$ for **e** and $\left(\begin{smallmatrix} n_3, & n_4 \\ n_7, & n_8 \end{smallmatrix}\right)$ for **f**, and the subscript S and T show the two-spin state of holes in the quantum dots indicated by bold numbers, respectively. The solid arrows show fast spin-conserving tunneling while the dashed arrows show suppressed tunneling due to PSB.

III. VIRTUAL GATE MATRIX

As mentioned in the main text, we use virtualized gates to independently control the chemical potential in each quantum dot. The virtual gate matrix is as follows:

$$
\begin{pmatrix} \mathrm{vP}_1 \\ \mathrm{vP}_2 \\ \mathrm{vP}_3 \\ \mathrm{vP}_4 \\ \mathrm{vP}_5 \\ \mathrm{vP}_6 \\ \mathrm{vP}_7 \\ \mathrm{vP}_8 \\ \mathrm{vB}_{12} \\ \mathrm{vB}_{23} \\ \mathrm{vB}_{34} \\ \mathrm{vB}_{56} \\ \mathrm{vB}_{67} \\ \mathrm{vB}_{78} \\ \mathrm{vB}_{15} \\ \mathrm{vB}_{26} \\ \mathrm{vB}_{37} \\ \mathrm{vB}_{48} \end{pmatrix} = \begin{pmatrix}
1 & 0.3 & 0.1 & 0.05 & 0.35 & 0.2 & 0.05 & 0.02 & 0.4 & 0.08 & 0 & 0.05 & 0.05 & 0 & 0.4 & 0.15 & 0 & 0 \\
0.15 & 1 & 0.3 & 0.05 & 0.05 & 0.25 & 0.05 & 0 & 0.3 & 0.2 & 0 & 0.05 & 0.1 & 0 & 0.1 & 0.2 & 0 & 0 \\
0.05 & 0.25 & 1 & 0.25 & 0 & 0.1 & 0.35 & 0.05 & 0 & 0.15 & 0.06 & 0 & 0.15 & 0.12 & 0 & 0 & 0.08 & 0.07 \\
0.02 & 0.05 & 0.35 & 1 & 0.02 & 0 & 0.15 & 0.35 & 0 & 0.05 & 0.06 & 0 & 0 & 0.11 & 0 & 0 & 0.03 & 0.28 \\
0.15 & 0.15 & 0.03 & 0.02 & 1 & 0.25 & 0.05 & 0.03 & 0.1 & 0.05 & 0 & 0.2 & 0.05 & 0.03 & 0.3 & 0 & 0.02 & 0 \\
0.1 & 0.2 & 0.1 & 0.05 & 0.2 & 1 & 0.2 & 0.05 & 0.1 & 0.1 & 0.05 & 0.1 & 0.25 & 0 & 0.1 & 0.1 & 0 & 0 \\
0.05 & 0.15 & 0.25 & 0.1 & 0.08 & 0.22 & 1 & 0.15 & 0 & 0.1 & 0.02 & 0.05 & 0.25 & 0.28 & 0.05 & 0 & 0.05 & 0.05 \\
0 & 0.03 & 0.2 & 0.25 & 0.03 & 0.05 & 0.45 & 1 & 0 & 0.02 & 0.025 & 0.02 & 0.05 & 0.4 & 0 & 0 & 0.03 & 0.22 \\
0 & 0 & 0 & 0 & 0 & 0 & 0 & 0 & 1 & 0 & 0 & 0 & 0 & 0 & 0 & 0 & 0 & 0 \\
0 & 0 & 0 & 0 & 0 & 0 & 0 & 0 & 0 & 1 & 0 & 0 & 0 & 0 & 0 & 0 & 0 & 0 \\
0 & 0 & 0 & 0 & 0 & 0 & 0 & 0 & 0 & 0 & 1 & 0 & 0 & 0 & 0 & 0 & 0 & 0 \\
0 & 0 & 0 & 0 & 0 & 0 & 0 & 0 & 0 & 0 & 0 & 1 & 0 & 0 & 0 & 0 & 0 & 0 \\
0 & 0 & 0 & 0 & 0 & 0 & 0 & 0 & 0 & 0 & 0 & 0 & 1 & 0 & 0 & 0 & 0 & 0 \\
0 & 0 & 0 & 0 & 0 & 0 & 0 & 0 & 0 & 0 & 0 & 0 & 0 & 1 & 0 & 0 & 0 & 0 \\
0 & 0 & 0 & 0 & 0 & 0 & 0 & 0 & 0 & 0 & 0 & 0 & 0 & 0 & 1 & 0 & 0 & 0 \\
0 & 0 & 0 & 0 & 0 & 0 & 0 & 0 & 0 & 0 & 0 & 0 & 0 & 0 & 0 & 1 & 0 & 0 \\
0 & 0 & 0 & 0 & 0 & 0 & 0 & 0 & 0 & 0 & 0 & 0 & 0 & 0 & 0 & 0 & 1 & 0 \\
0 & 0 & 0 & 0 & 0 & 0 & 0 & 0 & 0 & 0 & 0 & 0 & 0 & 0 & 0 & 0 & 0 & 1
\end{pmatrix} \begin{pmatrix} \mathrm{P}_1 \\ \mathrm{P}_2 \\ \mathrm{P}_3 \\ \mathrm{P}_4 \\ \mathrm{P}_5 \\ \mathrm{P}_6 \\ \mathrm{P}_7 \\ \mathrm{P}_8 \\ \mathrm{B}_{12} \\ \mathrm{B}_{23} \\ \mathrm{B}_{34} \\ \mathrm{B}_{56} \\ \mathrm{B}_{67} \\ \mathrm{B}_{78} \\ \mathrm{B}_{15} \\ \mathrm{B}_{26} \\ \mathrm{B}_{37} \\ \mathrm{B}_{48} \end{pmatrix}
$$

IV. ASYMMETRY IN MEASURED QUBIT ENERGY SPECTRUM

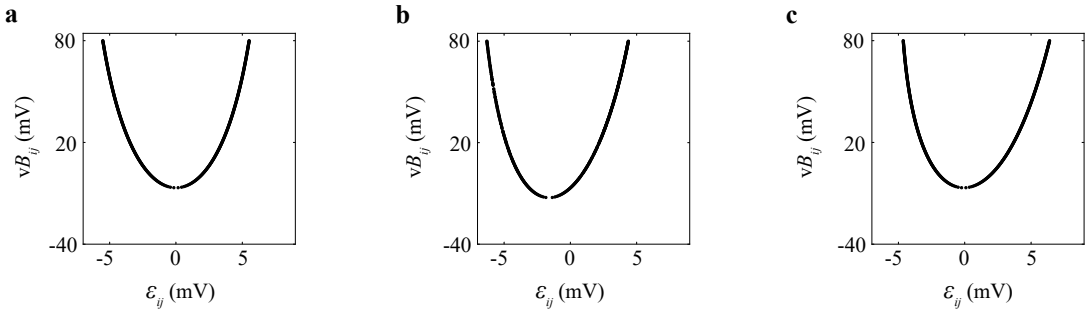

FIG. 3. **a**, Simulated parabola-like curve of the energy spectroscopy as a function of detuning ε_{ij} and barrier voltage vB_{ij} with a standard single-qubit Hamiltonian. **b**, Simulated asymmetrical curve by considering a detuning dependent g-factor. **c**, Simulated asymmetrical curve by considering a linear change of detuning offset as a function of vB_{ij}.

In Fig. 1 of the main text, we show energy spectrums of the S-T_- qubits and mention that the asymmetry of the parabola-like curve may be caused by the detuning-dependent g-factor or an imperfect virtualization of the barrier gate. Here we do a numerical simulation to determine their effects. The results are shown in Fig. 3a-c, which compares the standard energy spectrum (a) with the one with a detuning dependent g-factor (b) and that with imperfect virtualization (c). To numerically simulate these curves, we use the single-qubit Hamiltonian (13) and a relationship of $J = 2t^2U/(U^2 - \varepsilon^2)$. For the parameters, we use $U = 295$ GHz, $\overline{g} = 0.33$, $B = 10$ mT and $\Delta_{ST_-} = 16$ MHz. For the effect of g-factor change, we use a linear change of $\overline{g} = 0.19$-0.47 as a function of detuning, while for the effect of imperfect virtualization, we use a linear variation of detuning offset ε_0 as a function of the barrier gate voltage vB_{ij}, which changes in the range of -0.88 - 0.44 mV when vB_{ij} is changed from 80 to -40 mV. The variation of g-factor is a bit far away from the values reported in a similar device, where they report a change of 0.21-0.29 as a function of detuning [1]. But the 1% variation of ε_0 is plausible considering the imperfect virtualization. Still, the observed asymmetrical curve in the main text may result from their combined effects.

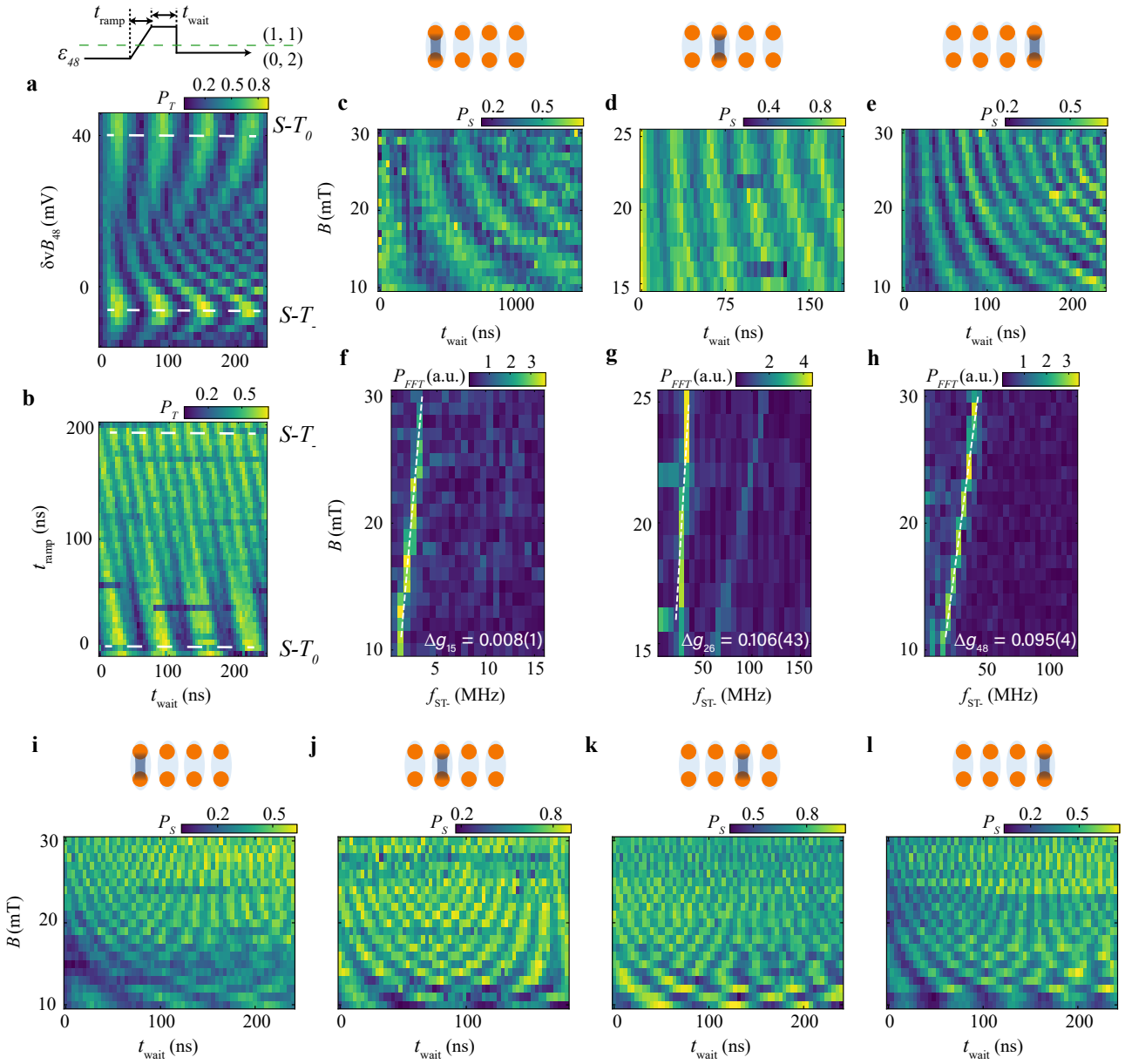

FIG. 4. **a**,**b**, Measured singlet-triplet oscillations of DQD 4-8 using a square pulse with a ramp-in time t_{ramp} and waiting time t_{wait}. **a**, Measured triplet probabilities as a function of t_{wait} and the barrier voltage amplitude $\delta \mathrm{vB}_{48}$ with $t_{\mathrm{ramp}} = 20$ ns. **b**, Measured triplet probabilities as a function of t_{wait} and t_{ramp} with $\delta \mathrm{vB}_{48} = 40$ mV. **c-e**, Measured singlet probabilities P_S as a function of t_{wait} and the magnetic field strength B for Q1 (**c**), Q2 (**d**), and Q4 (**e**) under S-T_0 control. Here t_{ramp} is set to zero to suppress unwanted S-T_- oscillations. **f-h**, The fast Fourier transforms of the data in **c-e**, with a signal that can be line-fitted using the g-factor difference Δg_{ij} of two dots. **i-l**, Measured singlet probabilities P_S of Q1 (**i**), Q2 (**j**), Q3 (**k**), and Q4 (**l**) as a function of t_{wait} and magnetic field strength B. These qubits are under S-T_- control with $t_{\mathrm{ramp}} = 100$ ns.

V. S-T_0 AND S-T_- OSCILLATIONS

In the main text, we discuss the coherent control of S-T_- qubits. Actually, by operating the DQD with different exchange couplings and ramping times, we can also encode a qubit in the S-T_0 subspace. Fig. 4a and b use Q4 as an example explaining how we transition from S-T_- to S-T_0 oscillations. As mentioned in the main text, a block pulse with 20-nanosecond ramp time (t_{ramp}) from (0,2) to (1,1) is adiabatic with respect to the S-T_0 splitting but

nonadiabatic with respect to the S-T_- anticrossing. Therefore, we can drive x-rotations of S-T_- qubits when this pulse amplitude reaches the detuning center where $J(\varepsilon_{ij}=0)\sim\overline{E_z}$ (see Fig. 1d in the main text). However, when we increase the barrier voltage change $\delta \mathrm{v}B_{48}$ until $J(\varepsilon_{ij}=0)<\overline{E_z}$ (see Fig. 1c in the main text), the S-T_- anticrossings are no longer at the detuning center, therefore the same pulse cannot produce the x-axis oscillations of S-T_- qubits. Moreover, under this condition, the energy gap of the S-T_0 splitting is reduced and the 20-nanosecond ramp time is no longer adiabatic with respect to the S-T_0 splitting. As a result, the singlet state will nutate between the S and T_0 states under the control of the Zeeman energy difference between the two dots ΔE_z. The corresponding experimental result is shown in Fig. 4a, where we can observe clear S-T_- oscillations with $\delta \mathrm{v}B_{48}\sim -10$ mV and S-T_0 oscillations with $\delta \mathrm{v}B_{48}\sim 40$ mV.

This crossover between S-T_- and S-T_0 oscillations can also be tuned by changing t_{ramp}. At $\delta \mathrm{v}B_{48}=40$ mV, when we increase t_{ramp} until the pulse is adiabatic again with respect to the S-T_0 splitting, the S-T_0 oscillations can no longer be observed. However, such a long ramp time can rotate the initial state and make z-axis control of S-T_- qubits visible again [3]. Therefore, we also observe a transition of S-T_0 oscillations and S-T_- oscillations as a function of t_{ramp} in experiments. As shown in Fig. 4b, S-T_0 oscillations disappear and S-T_- oscillations are recovered when t_{ramp} surpasses 100 ns.

Using the method above, we measured S-T_0 oscillations as a function of the magnetic field with $t_{\mathrm{ramp}}=0$ ns for Q1, Q2, and Q4, as shown in Fig. 4c-e. The corresponding fast Fourier transforms (FFT) are shown in Fig. 4(f-h), from which we extract g-factor differences Δg as 0.008(1), 0.106(43), and 0.095(4) for Q1, Q2, and Q4, respectively. For Q3, we didn't find S-T_0 oscillations, which may be because the corresponding Δg is too low to detect. We also measured S-T_- oscillations as a function of the magnetic field with $t_{\mathrm{ramp}}=100$ ns for Q1-Q4, as shown in Fig. 4i-l, and extract $\overline{g}=0.33(1)-0.37(1)$ (see Fig. 2m in the main text).

VI. ADDITIONAL CONTEXT AND DATA OF SWAP OPERATIONS

For the SWAP interaction of Q3-Q4, we also scanned the oscillations over a wider range of detuning compared to the data of Fig. 3f in the main text. The result is shown in Fig. 5a. There are three sets of oscillations from left to right, where the rightmost corresponds to SWAP oscillations of Q3-Q4 discussed in the main text, the middle oscillations correspond to a single-qubit operation of Q4, and the leftmost is also a set of SWAP oscillations but with a very slow oscillation speed, which corresponds to a smaller interqubit coupling than the rightmost one due to the detuning arrangement (see the leftmost anticrossing in Fig. 3b of the main text). These features can all be qualitatively understood using Fig. 3b in the main text. However, to quantitatively simulate its behavior, the contribution of anisotropic exchange couplings may be needed.

We also tried sequential readout after SWAP oscillations of Q2-Q3. By pulsing the barrier gate $\delta \mathrm{v}B_{26}$ to -60 mV, we can measure Q3 (during 20 μs) and simultaneously keep Q2 in the center of (1,1) with sufficiently large J, where the Hamiltonian eigenbasis corresponds to the qubit readout basis [2, 4, 5]. Afterwards, Q2 is measured in the same sequence. Thus, the two-qubit joint probabilities P_{SS}, P_{TS}, P_{ST} and P_{TT} of Q2 and Q3, can be acquired simultaneously. By initializing Q2-Q3 into $|T_-S\rangle$, we observe out-of-phase oscillations of P_{TS} and P_{ST} under SWAP interactions in Fig. 5b. For comparison, if Q2-Q3 is initialized into $|SS\rangle$, we do not observe any oscillations, as expected, except for the single-qubit rotations at low detuning, as shown in Fig. 5c. We don't observe leakage to $|TT\rangle$, which is expected given that, in this regime, the states $|TT\rangle$ are far away in energy from the other states, see Fig. 3b in the main text.

VII. PULSE SCHEME AND CALIBRATION FOR QUANTUM STATE TRANSFER

The detailed pulse scheme for quantum state transfer in the main text is shown in Fig. 6a. We initialize Q1-Q4 in the $\left(\begin{smallmatrix}2&0&2&0\\0&2&0&2\end{smallmatrix}\right)$ regime and then diabatically pulse to the $\left(\begin{smallmatrix}1&1&1&1\\1&1&1&1\end{smallmatrix}\right)$ regime, preserving four singlets. At this point, the detuning of Q1 and Q3 is set close to the (1,1)-(2,0) transition and that of Q4 close to the (1,1)-(0,2) transition in order to stay away from the S-T_- anticrossing. This ensures that these three qubits remain in the singlet state. The detuning of Q2 is set to zero such that Q2 rotates around its x axis to $|T_-\rangle$. Then we pulse the detunings and barrier gates of Q1-Q2 to initiate a SWAP interaction for a duration t_{wait}, after which we transfer the state of Q2 to Q4 by performing sequential SWAP operations of Q2-Q3 and Q3-Q4. Finally, we pulse Q4 to zero detuning to kickstart single-qubit evolution around the x-axis for a duration t_{Q4}. For readout, we pulse Q1-Q4 into $\left(\begin{smallmatrix}1&1&1&0\\1&1&1&2\end{smallmatrix}\right)$ where we perform PSB readout of Q4. The detunings of Q1-Q3 are set to zero while Q4 is read out, but this will not affect the readout since Q4 is protected by a very large J in the readout window.

Before the quantum state transfer experiment, we confirm the operation of the individual SWAP gates by performing a single-qubit rotation of one qubit and measuring its state using the other after a SWAP gate. Some results are

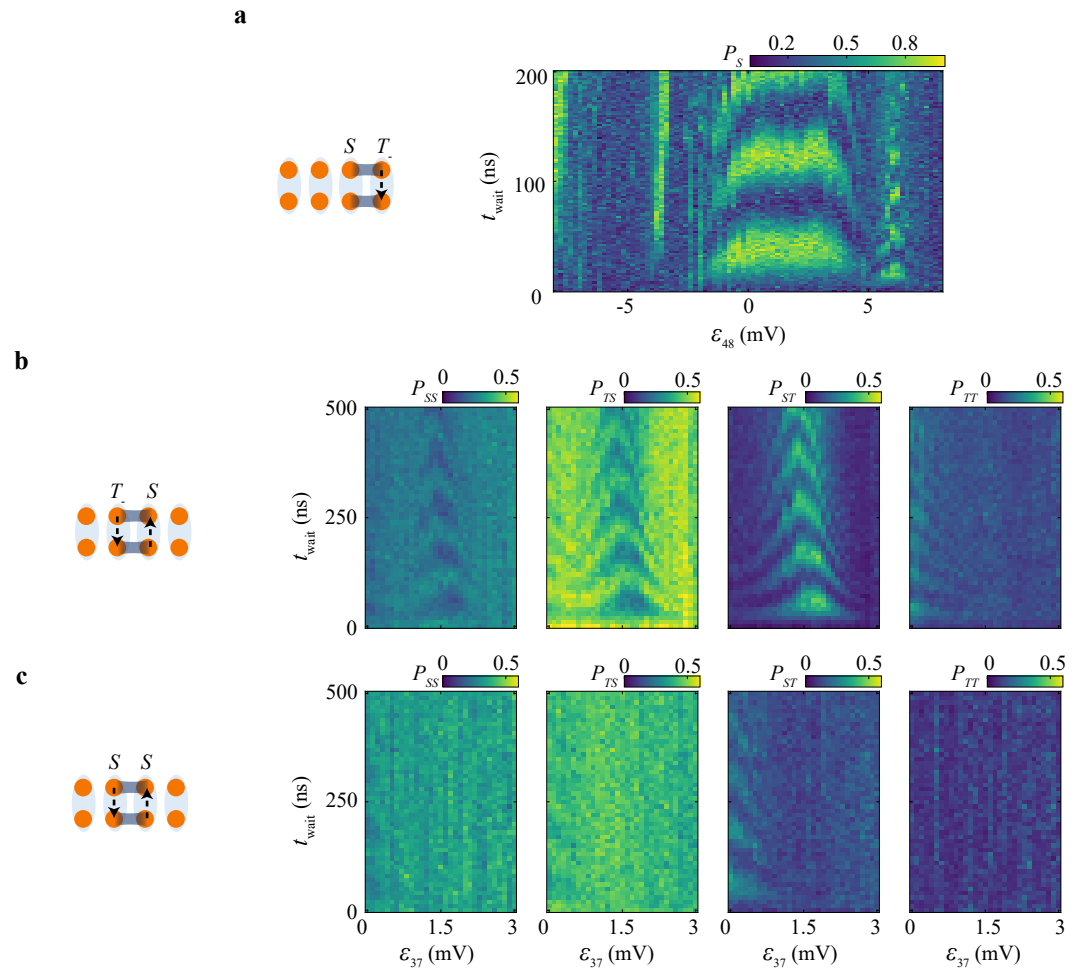

FIG. 5. **a**, Measured triplet probabilities of Q4 as a function of waiting time t_{wait} and the detuning of Q4, ε_{48}, after initializing Q3-Q4 into $|ST_{-}\rangle$. **b**,**c**, Sequentially measured probabilities P_{SS}, P_{TS}, P_{ST} and P_{TT} of Q2 and Q3 as a function of t_{wait} and the detuning of Q3, ε_{37}, after initializing Q2-Q3 into $|T_{-}S\rangle$ (**b**) and $|SS\rangle$ (**c**). The data is acquired at a different magnetic field $B = 5$ mT but the detuning arrangement is similar to the results in the main text. In **b**, the out-of-phase signals in P_{TS} and P_{ST} observed around $\varepsilon_{37} = 1.5$ mV are the result of the SWAP oscillations between these two qubits. A similar signal to P_{TS} but with lower visibility is observed in P_{SS}, which can be explained by the higher triplet readout error for Q2 than for Q3.

shown in Fig. 6b and c, where we perform this test for Q3-Q4 and Q2-Q3, respectively. Fig. 6d shows a result where Q1 is rotated and the measured qubit is Q4 following three consecutive SWAP gates from Q1 to Q4. A comparison of the direct readout of Q1 is shown in Fig. 6e, with similar oscillations to that of Fig. 6d at similar detuning voltages. These results demonstrate the SWAP gates are of sufficient quality to allow quantum state transfer across the entire array.

VIII. A THEORETICAL MODEL FOR THE SWAP OPERATION

Holes confined in quantum dots are well described by the conventional Fermi-Hubbard model [6]. In the presence of a finite magnetic field and spin-orbit interaction, the Fermi-Hubbard model can be written as:

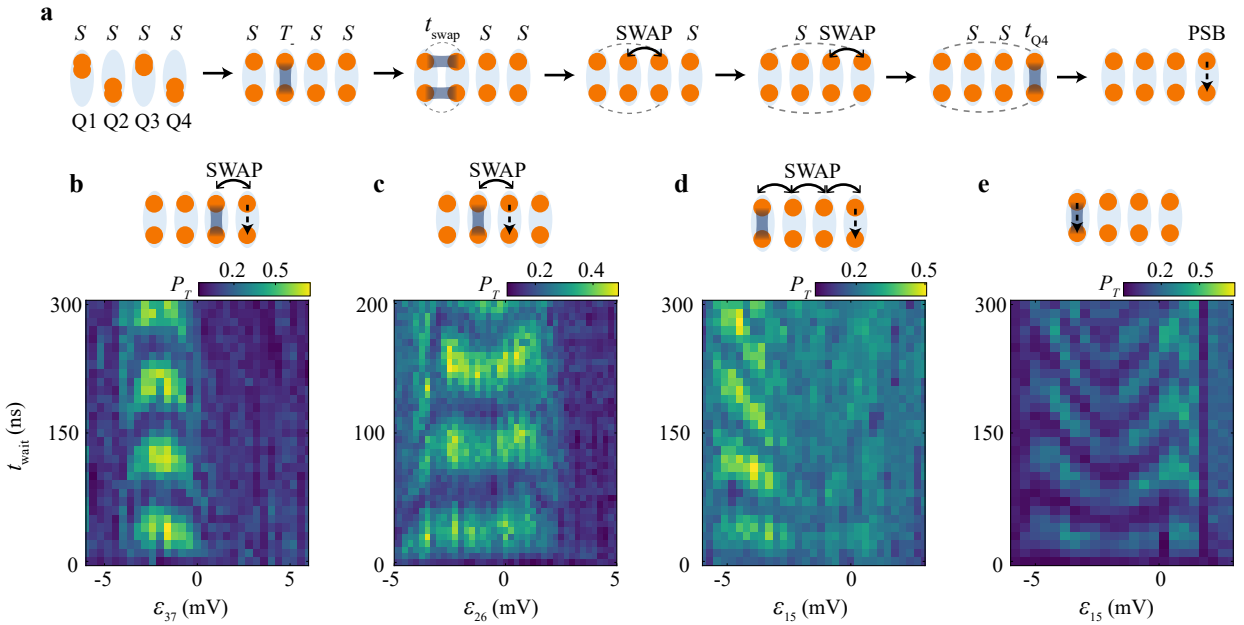

FIG. 6. **a**, Schematic representation of the different steps in the quantum-state-transfer experiment of Fig. 4 of the main text. The gray dashed curves indicate potential entanglement between two qubits. The black curved double-arrow refers to a SWAP gate that is intended to transfer information from one qubit to the next. **b**, Measured triplet probabilities of Q4 as a function of waiting time $t_{\rm wait}$ and detuning of Q3, ε_{37}. The inset illustrates that we control Q3 to perform an x-rotation with a time $t_{\rm wait}$ and subsequently perform a SWAP gate of Q3-Q4 and measure Q4 using PSB. **c**, Measured triplet probabilities of Q3 as a function of $t_{\rm wait}$ and detuning of Q2, ε_{26}. The inset illustration is similar to that in **b** but with single-qubit control of Q2, a subsequent SWAP gate of Q2-Q3 and PSB measurement of Q3. **d**, Measured triplet probabilities of Q4 as a function of $t_{\rm wait}$ and the detuning of Q1, ε_{15}. The inset shows that we perform an x-rotation of Q1 with a time $t_{\rm wait}$ followed by three consecutive SWAP gates to transfer the state of Q1 to Q2, Q3 and Q4, after which we measure Q4 using PSB. **d** has lower visibility on the right-hand side of the figure compared to its left-hand side, which can be attributed to a possible parameter shift of the consecutive SWAP gates by low-frequency charge noise after the left part was scanned. **e**, Direct readout of Q1 with the same single-qubit control as in **d**.

$$H_{\rm FH} = \sum_{i=1}\Big[\mu_i n_i + \mu_B \boldsymbol{B}\cdot\tilde{\mathcal{G}}_i\boldsymbol{S}_i\Big] + \sum_{i=1}\frac{\tilde{U}_i}{2}n_i(n_i-1) + \sum_{\langle i,j\rangle}V_{ij}n_in_j + \sum_{\sigma=\uparrow,\downarrow}\Big(\tilde{t}_{ij}c^\dagger_{i,\sigma}c_{j,\sigma}+\text{h.c.}\Big) + \sum_{\sigma=\uparrow,\downarrow}\Big(\tilde{t}_{\text{SO},ij}c^\dagger_{i,\sigma}c_{j,\bar{\sigma}}+\text{h.c.}\Big). \tag{1}$$

Here, h.c. denotes hermitian conjugate, $\bar{\sigma}$ the opposite spin state of σ, the operator $c^\dagger_{i,\sigma}$ ($c_{i,\sigma}$) creates (annihilates) a hole in QD i with spin $\sigma=\uparrow,\downarrow$, $n_i \equiv \sum_\sigma c^\dagger_{i,\sigma}c_{i,\sigma}$ is the charge number operator, and $\boldsymbol{S} = (S_{x,i}, S_{y,i}, S_{z,i})^T$ is the vector consisting of the spin matrices

$$S_{x,i} = \frac{\hbar}{2}(c^\dagger_{i,\uparrow}c_{i,\downarrow} + c^\dagger_{i,\downarrow}c_{i,\uparrow}) \tag{2}$$

$$S_{y,i} = -i\frac{\hbar}{2}(c^\dagger_{i,\uparrow}c_{i,\downarrow} - c^\dagger_{i,\downarrow}c_{i,\uparrow}) \tag{3}$$

$$S_{z,i} = \frac{\hbar}{2}(c^\dagger_{i,\uparrow}c_{i,\uparrow} - c^\dagger_{i,\downarrow}c_{i,\downarrow}). \tag{4}$$

The first line in Hamiltonian (1) describes the hole energies, i.e., μ_i denotes the chemical potential in QD i, $\tilde{U}_i$ is the Coulomb repulsion for doubly occupying the i-th QD, V_{ij} is the Coulomb repulsion of two holes occupying neighboring QDs i and j, μ_B is Bohr's magneton, and $\tilde{\mathcal{G}}_i$ is the quantum dot g-tensor. The second line describes the hopping

terms between neighboring sites denoted by the spin-conserving tunnel matrix elements $\tilde{t}_{ij}$ and spin-non-conserving tunnel matrix elements $\tilde{t}_{\mathrm{SO},ij}$. Note, that this notation is consistent with Refs. [7, 8] as $\tilde{t}_{ij}$ and $\tilde{t}_{\mathrm{SO},ij}$ can be complex in general.

Single-qubit Hamiltonian

Considering only two neighboring quantum dots, the Hamiltonian can be simplified by transforming into the spin-orbit frame [8]. Intuitively, since the spin-orbit interaction only rotates the spin during tunneling, local spin rotations can always "unwind" the rotation. As a consequence of the spin-orbit interaction, the g-tensor of quantum dot i is rotated as $\tilde{\mathcal{G}}_i \to R_i\tilde{\mathcal{G}}_i \equiv \mathcal{G}_i$, and the tunnel coupling is renormalized as $t = \sqrt{|\tilde{t}|^2 + |\tilde{t}_{\mathrm{SO}}|^2}$ [8].

Hamiltonian The respective Hamiltonian in the basis $\{S(2,0),\ S(0,2),\ S(1,1),\ T_-(1,1),\ T_0(1,1),\ T_+(1,1)\}$ of the spin-orbit frame reads

$$H_{\mathrm{DQD}} = \begin{bmatrix} U+\varepsilon & 0 & \sqrt{2}t & 0 & 0 & 0 \\ 0 & U-\varepsilon & \sqrt{2}t & 0 & 0 & 0 \\ \sqrt{2}t & \sqrt{2}t & 0 & \frac{\Delta E_x - i\Delta E_y}{\sqrt{2}} & \Delta E_z & -\frac{\Delta E_x + i\Delta E_y}{\sqrt{2}} \\ 0 & 0 & \frac{\Delta E_x + i\Delta E_y}{\sqrt{2}} & -\bar{E}_z & \frac{\bar{E}_x + i\bar{E}_y}{\sqrt{2}} & 0 \\ 0 & 0 & \Delta E_z & \frac{\bar{E}_x - i\bar{E}_y}{\sqrt{2}} & 0 & \frac{\bar{E}_x + i\bar{E}_y}{\sqrt{2}} \\ 0 & 0 & \frac{-\Delta E_x + i\Delta E_y}{\sqrt{2}} & 0 & \frac{\bar{E}_x - i\bar{E}_y}{\sqrt{2}} & \bar{E}_z \end{bmatrix}. \tag{5}$$

Here, we introduce the energy detuning $\varepsilon = \mu_1 - \mu_2$, and the average and difference in Zeeman energy for a fixed magnetic field direction, $2\hat{E}_\xi = \mu_B \boldsymbol{B}(\mathcal{G}_1 + \mathcal{G}_2)\hat{\xi}$ and $2\Delta E_\xi = \mu_B \boldsymbol{B}(\mathcal{G}_1 - \mathcal{G}_2)\hat{\xi}$, where $\hat{\xi}$ is the unit vector along axis $\xi = x, y, z$. We note that in our experiment we only have access to the energies and not the individual g-tensors due to the lack of access to a vector magnet.

Simulations To compute the single-qubit energy spectra in the main text (Fig. 1c-e), we use Hamiltonian (1) assuming only real tunnel matrix elements. Explicitly, we set the spin-conserving tunneling as $\widetilde{t} = 1.2,\ 1.86,\ 2.4$ GHz, the spin-non-conserving tunneling as $\widetilde{t}_{\mathrm{SO}} = 10$ MHz, and $U = 300$ GHz, $B = |\boldsymbol{B}| = 10$ mT, $\overline{g} = |\mathcal{G}_1 + \mathcal{G}_2|/2 = 0.33$, $\Delta g = |\mathcal{G}_1 - \mathcal{G}_2|/2 = 0.008$, and with all other components of the g-tensors set to zero.

Effective qubit Hamiltonian To separate the spin dynamics from the charge dynamics, we now restrict ourselves to the subspace spanned by the spin states $\{S(1,1),\ T_-(1,1),\ T_0(1,1),\ T_+(1,1)\}$. This can be done either by block-diagonalizing via Schrieffer-Wolff perturbation theory [9] or by diagonalizing the singlet sector spanned by $\{S(2,0),\ S(0,2),\ S(1,1)\}$ with a subsequent projection or block-diagonalization [8]. Regardless of the chosen method, the resulting Hamiltonian has the form of a generalized Heisenberg Hamiltonian

$$H_{\mathrm{DQD}} = \begin{bmatrix} J_0 & \frac{\Delta E_x - i\Delta E_y}{\sqrt{2}} & \Delta E_z & -\frac{\Delta E_x + i\Delta E_y}{\sqrt{2}} \\ \frac{\Delta E_x + i\Delta E_y}{\sqrt{2}} & -\bar{E}_z & \frac{\bar{E}_x + i\bar{E}_y}{\sqrt{2}} & 0 \\ \Delta E_z^* & \frac{\bar{E}_x - i\bar{E}_y}{\sqrt{2}} & 0 & \frac{\bar{E}_x + i\bar{E}_y}{\sqrt{2}} \\ \frac{-\Delta E_x + i\Delta E_y}{\sqrt{2}} & 0 & \frac{\bar{E}_x - i\bar{E}_y}{\sqrt{2}} & \bar{E}_z \end{bmatrix}, \tag{6}$$

where J_0 is the exchange interaction. In the regime of single dot occupation, $|t| \ll |U \pm \epsilon|$, the exchange interaction can be approximated by [9]

$$J = \frac{2t^2 U}{U^2 - \varepsilon^2}. \tag{7}$$

We note that during the transformation $\Delta E_{x,y,z} \to \Delta E'_{x,y,z}$ is renormalized by the charge-state admixture [8, 10]. To improve readability and because it has no practical consequences, we immediately drop the prime.

Starting from Hamiltonian (6) we can now construct the qubit Hamiltonian. The $|0\rangle \equiv |S\rangle = S(1,1)$ qubit state is defined via the PSB readout mechanism. We find the second qubit state by diagonalizing the triplet sector spanned by $\{T_-(1,1),\ T_0(1,1),\ T_+(1,1)\}$. Fortunately, the transformation can be parameterized as $e^{-i\boldsymbol{v}\cdot\boldsymbol{S}^0/\hbar}$, where $\boldsymbol{v}$ is a real vector and $\boldsymbol{S}^0$ is a vector containing the spin-0 matrices

$$S_x^0 = \frac{1}{2}(S_{x,1} + S_{x,2}) \tag{8}$$

$$S_y^0 = \frac{1}{2}(S_{y,1} + S_{y,2}) \tag{9}$$

$$S_z^0 = \frac{1}{2}(S_{z,1} + S_{z,2}). \tag{10}$$

The $|1\rangle \equiv |T_-\rangle$ qubit state is then consequently given by the lowest-energy state. The final qubit Hamiltonian reads

$$\tilde{H}_{ST_-} = \begin{bmatrix} -J & \frac{\Delta_{ST_-} e^{i\phi_{ST_-}}}{2} \\ \frac{\Delta_{ST_-} e^{-i\phi_{ST_-}}}{2} & -\overline{E}_z \end{bmatrix}. \tag{11}$$

In lowest-order perturbation theory the exchange energy $J = J_0$, the average Zeeman splitting $\overline{E}_z = \sqrt{\bar{E}_x^2 + \bar{E}_y^2 + \bar{E}_z^2}$, and the spin-orbit coupling reads

$$\Delta_{\mathrm{SO}} e^{i\phi_{ST_-}} = \sqrt{2}\frac{\Delta E_z \left(\bar{E}_x^2 + \bar{E}_y^2\right) - \bar{E}_z(\Delta E_x \bar{E}_x + \Delta E_y \bar{E}_y)}{\overline{E}_z(\hat{E}_x - i\bar{E}_y)} + \sqrt{2}i\frac{\Delta E_x \bar{E}_y - \Delta E_y \bar{E}_x}{(\hat{E}_x - i\bar{E}_y)}. \tag{12}$$

To arrive at the single-qubit Hamiltonian in the main text, we apply the local phase transformation $U_\phi = \exp(-i\phi_{ST_-}(|0\rangle\langle 0| - |1\rangle\langle 1|)/2)$

$$H_{ST_-} = U_\phi \tilde{H}_{ST_-} U_\phi^\dagger = \begin{bmatrix} -J & \frac{\Delta_{ST_-}}{2} \\ \frac{\Delta_{ST_-}}{2} & -\overline{E}_z \end{bmatrix}, \tag{13}$$

We remark that a more accurate Hamiltonian can be computed recursively using perturbation theory for a sufficiently large spectral gap [11]. We also remark that leakage outside the qubit subspace can be strongly suppressed using optimal control theory and Hamiltonian engineering.

Decoherence times

Charge noise and nuclear spin noise are ubiquitous in germanium semiconductor devices. Due to the low-frequency nature of both types of noise, they can be approximately modeled as quasistatic fluctuations of input parameters, giving rise to pure dephasing. Furthermore, we ignore in our analysis any energy relaxation mechanism, which is a good approximation for spin qubits [6]. Hamiltonian (13) under weak low-frequency noise thus becomes [12]

$$H_{ST_-} = \begin{bmatrix} -J - \delta J & \frac{\Delta_{ST_-} + \delta\Delta_x - i\delta\Delta_y}{2} \\ \frac{\Delta_{ST_-} + \delta\Delta_x + i\delta\Delta_y}{2} & -\overline{E}_z - \delta\overline{E}_z \end{bmatrix}, \tag{14}$$

where δ denotes fluctuations. Note that there are two off-diagonal contributions $\delta\Delta_x$ and $\delta\Delta_y$ that arise from the complex quantity $\Delta_{ST_-} e^{i\phi_{ST_-}}$. Assuming quasi-static noise (or low-frequency noise within the adiabatic approximation) the qubit resonance frequency is modulated by noise as follows

$$\hbar\omega_q = \sqrt{4(J - \overline{E}_z)^2 + \Delta_{ST_-}^2} \to \sqrt{4(J - \overline{E}_z + \delta J - \delta\overline{E}_z)^2 + (\Delta_{ST_-} + \delta\Delta_x)^2 + \delta\Delta_y^2}. \tag{15}$$

The S-T_- qubit is operated in two regimes which we separately discuss.

Dephasing during rotations around the x-axis For single-qubit x-rotations, we operate at $J = \overline{E}_z$ and we can expand Eq. (15) up to first order

$$\hbar\omega_q^x = \Delta_{ST_-} + \delta\Delta_x + \mathcal{O}(\delta^2) \tag{16}$$

to find the dominating contributions. Assuming Gaussian distributed noise, the decoherence time in the x-axis rotation regime is then given by

$$T_x^* = \frac{1}{\sqrt{2}\sigma_{\Delta_x}}, \tag{17}$$

where $\sigma^2_{\Delta_x} = \langle \delta\Delta_x^2 \rangle - \langle \delta\Delta_x \rangle^2$ is the standard deviation of the $\delta\Delta_x$ noise. Since $\Delta E_\xi \propto B$ and $\overline{E}_\xi \propto B$ for $\xi = x, y, z$, we expect $T_x^* \propto B^{-1}$ for an in-plane magnetic field [13, 14]. Therefore, operating at small magnetic fields is beneficial for x-gates.

Dephasing during rotations around the z-axis For single-qubit z-rotations, we operate at $|J - \overline{E}_z| \gg \Delta_{ST_-}$ and we can expand Eq. (15) up to first order

$$\hbar\omega_q^z = |J - \overline{E}_z + \delta J - \delta\overline{E}_z| + \mathcal{O}(\delta^2) \tag{18}$$

to find the dominating contributions. Assuming Gaussian distributed noise the decoherence time in the z-axis rotation regime is then given by

$$T_z^* = \frac{1}{\sqrt{2}\sigma_{J,\overline{E}_z}(1+c)}, \tag{19}$$

where $\sigma^2_{\sigma_{J,\overline{E}_z}} = \langle (\delta J - \delta\overline{E}_z)^2 \rangle - \langle (\delta J - \delta\overline{E}_z) \rangle^2$ is the standard deviation of the noise difference, $c = \mathrm{cov}(J, \overline{E}_z)/(\sigma_J \sigma_{\overline{E}_z})$ the noise correlation factor, $\mathrm{cov}(J, \overline{E}_z)$ the covariance, and σ_J ($\sigma_{\overline{E}_z}$) the standard deviation of the individual fluctuations δJ and $\delta\overline{E}_z$. Since $\overline{E}_z \propto B$, operating at small magnetic fields can suppress fluctuations of the Zeeman splitting, giving rise to $T_z^* = \frac{1}{\sqrt{2}\sigma_J}$. In contrast to T_x^*, thus, T_z^* is not suppressed at small magnetic fields. This is consistent with the observations in the main text that $T_z^* < T_x^*$.

Two-qubit Hamiltonian

The derivation of the Hamiltonian of two coupled S-T_- qubits is analogous to that of the single-qubit Hamiltonian. The first step is separating the spin and charge degree of freedom, resulting in a generalized Heisenberg Hamiltonian. We give explicit expressions for the two-qubit Hamiltonian for two different architectures, a simplified architecture with single connectivity and the design from the experiment.

Linear chain with a single inter-qubit tunnel (exchange) coupling and isotropic g-tensor up to a scaling. In this case, the multi-qubit Hamiltonian is given by

$$H_{\mathrm{FH}} = \sum_{i=1} \mu_B g_i B S_{z,i} + \sum_{i=1} \frac{\Delta_{ST_-,i}}{\hbar} S_x + \sum_{\langle i,j \rangle} + J_{ij} \left(\frac{\boldsymbol{S}_i \cdot \boldsymbol{S}_j}{\hbar^2} - \frac{1}{4} \right), \tag{20}$$

where $\langle i, j \rangle$ denotes neighboring quantum dots. Projected on the two-qubit basis $\{|S,S\rangle, |S,T_-\rangle, |T_-,S\rangle, |T_-,T_-\rangle\}$ the two-qubit Hamiltonian reads

$$H_{2\mathrm{Q}} = H_{\mathrm{Q1}} + H_{\mathrm{Q2}} + H_{\mathrm{coup,iso}} \tag{21}$$

with

$$H_{\mathrm{Q1}} + H_{\mathrm{Q2}} = \begin{bmatrix} -J_{ij} - J_{kl} & \frac{\Delta_{\mathrm{SO},kl}}{2} & \frac{\Delta_{\mathrm{SO},ij}}{2} & 0 \\ \frac{\Delta_{\mathrm{SO},kl}}{2} & -J_{ij} - \overline{E}_{z,kl} & 0 & \frac{\Delta_{\mathrm{SO},ij}}{2} \\ \frac{\Delta_{\mathrm{SO},ij}}{2} & 0 & -\overline{E}_{z,ij} - J_{kl} & \frac{\Delta_{\mathrm{SO},kl}}{2} \\ 0 & \frac{\Delta_{\mathrm{SO},ij}}{2} & \frac{\Delta_{\mathrm{SO},kl}}{2} & -\overline{E}_{z,ij} - \overline{E}_{z,kl} \end{bmatrix}, \tag{22}$$

$$H_{\mathrm{coup,iso}} = \frac{1}{2} \begin{bmatrix} -J_{\mathrm{coup}} & 0 & 0 & 0 \\ 0 & -J_{\mathrm{coup}} & J_{\mathrm{coup}} & 0 \\ 0 & J_{\mathrm{coup}} & -J_{\mathrm{coup}} & 0 \\ 0 & 0 & 0 & 0 \end{bmatrix}, \tag{23}$$

Here the subscripts indicate the sites i, j, k and l, respectively. Note that this Hamiltonian is identical to the Hamiltonian used in the main text up to an energy offset that corresponds to a global phase shift.

From a quantum information point of view, the isotropic exchange Hamiltonian (23) generates a universal two-qubit gate. More precisely, the Hamiltonian generates a SWAP + iSWAP gate. This can be visualized through the symmetry of the system: since the isotropic exchange interaction is given by the projector on the singlet subspace, the $|T_-T_-\rangle\langle T_-T_-|$ matrix element of the two-qubit interaction has to be zero.

Ladder with two inter-qubit tunnel (exchange) couplings and anisotropic g-tensors. This is the architecture used in the present device. Consequently, the Hamiltonian cannot be cast into Eq. (20) and an additional rotation of the spin has to be taken into account [8]. Fortunately, the "additional" rotation from the exchange interaction can be absorbed into the rotation caused by the differences in g-tensor for a fixed magnetic field setting. In this case the total two-qubit Hamiltonian is given by

$$H_{2Q} = H_{Q1} + H_{Q2} + H_{\text{coup,iso}} + H_{\text{coup,SOI}}\ , \tag{24}$$

where the first three terms are given in Eqs. (22)-(23). The last term is caused by the spin-orbit interaction and is given by

$$H_{\text{coup,SOI}} = P_{2Q}U_{ij,kl}\left[\left(\frac{\boldsymbol{S}_i\cdot\mathcal{J}_{ik}\boldsymbol{S}_k}{\hbar^2}-\frac{1}{4}\right)+\left(\frac{\boldsymbol{S}_j\cdot\mathcal{J}_{jl}\boldsymbol{S}_l}{\hbar^2}-\frac{1}{4}\right)\right]U^{\dagger}_{ij,kl}P_{2Q} - H_{\text{coup,iso}}, \tag{25}$$

$$= \frac{1}{2}\begin{bmatrix} 0 & 0 & 0 & J^{\text{SO}}_{\perp 2,ij,kl} \\ 0 & 0 & J^{\text{SO}}_{\perp 1,ij,kl} & J^{\text{SO}}_{a2,ij,kl} \\ 0 & J^{\text{SO},*}_{\perp 1,ij,kl} & 0 & J^{\text{SO}}_{a1,kl,ij} \\ J^{\text{SO},*}_{\perp 2,ij,kl} & J^{\text{SO},*}_{a2,ij,kl} & J^{\text{SO},*}_{a1,kl,jk} & -J^{\text{SO}}_{||,ij,kl} \end{bmatrix}, \tag{26}$$

where P_{2Q} is the projector on the two-qubit subspace,

$$U_{ij,kl} = U_{\phi_{ij}}U_{\phi_{kl}}e^{i\boldsymbol{v}_{ij}\cdot\boldsymbol{S}^0_{ij}/\hbar}\,e^{i\boldsymbol{v}_{kl}\cdot\boldsymbol{S}^0_{kl}/\hbar}, \tag{27}$$

is the combination of the single S-T_- qubit basis transformation from the previous section, and $\mathcal{J}_{ik(jl)}$ is the exchange tensor between the spins in quantum dot pair ik (jl) in the spin-orbit basis [8] of quantum dot pair ij and kl. We also note that the full characterization of all elements cannot be resolved with our current operation regime and measurement setup, as high-fidelity sequential spin readout is required. For example, the $J^{\text{SO}}_{\perp 2,ij,kl}$ term could be characterized in the regime where the energies of the $|SS\rangle$ and $|T_-T_-\rangle$ states are identical but energetically separated from the other states. Therefore, we consider for simplicity an isotropic model to describe the swapping dynamics which fits well to the observations.

Simulation of the two-qubit energy spectrum To compute the two-qubit energy spectrum between Q3 and Q4 in the main text (Fig. 3b), we use the Hamiltonian of (21) and Eq. (7) and the estimated single-qubit parameters at B = 10 mT. Explicitly, we use U_{Q3} = 290 GHz, U_{Q4} = 326 GHz, t_{Q3} = 3 GHz, t_{Q4} = 2.8 GHz, ε_{Q3} = -174 GHz, $\overline{g}_{Q3}$ = 0.37, $\overline{g}_{Q4}$ = 0.35, and assume for simplicity a homogeneous $\Delta_{\text{SO},ij} = \Delta_{\text{SO},kl}$ = 10 MHz. For the two-qubit interaction between Q3 and Q4, we use $H_{\text{coup,iso}}$ with $J_{\text{coup}} = (J_{ik} + J_{jl})/2$. We have estimated the inter-qubit exchange using t_{ik} = 2 GHz and t_{jl} = 0.4 GHz and $\varepsilon_{ik} = (\varepsilon_{ij} - \varepsilon_{kl} + \mu_0)/2$ and $\varepsilon_{jl} = (\varepsilon_{kl} - \varepsilon_{ij} + \mu_0)/2$ by assuming the difference between the chemical potential offsets of two qubits $\mu_0 = \mu_{ij} - \mu_{kl} = 0$.

Simulation of the state transfer For the simulation of the state transfer in the main text (Fig. 4b), we use the Hamiltonian of Eq. (23) for the SWAP operations with J_{coup} = 95 MHz and a single-qubit x-axis rotation frequency of Q4 of 13 MHz.

[1] Hendrickx, N. *et al.* A single-hole spin qubit. *Nat. Commun.* **11**, 3478 (2020).

[2] van Diepen, C. J. *et al.* Quantum simulation of antiferromagnetic Heisenberg chain with gate-defined quantum dots. *Phys. Rev. X.* **11**, 041025 (2021).

[3] Jirovec, D. *et al.* Dynamics of hole singlet-triplet qubits with large g-factor differences. *Phys. Rev. Lett.* **128**, 126803 (2022).

[4] Shulman, M. D. *et al.* Demonstration of entanglement of electrostatically coupled singlet-triplet qubits. *Science* **336**, 202–205 (2012).

[5] Wang, C.-A. *et al.* Probing resonating valence bonds on a programmable germanium quantum simulator. *npj Quantum Inf.* **9**, 58 (2023).
[6] Burkard, G., Ladd, T. D., Pan, A., Nichol, J. M. & Petta, J. R. Semiconductor spin qubits. *Rev. Mod. Phys.* **95**, 025003 (2023).
[7] Danon, J. & Nazarov, Y. V. Pauli spin blockade in the presence of strong spin-orbit coupling. *Phys. Rev. B* **80**, 041301 (2009).
[8] Geyer, S. *et al.* Two-qubit logic with anisotropic exchange in a fin field-effect transistor. *arXiv preprint arXiv:2212.02308* (2022).
[9] Burkard, G., Loss, D. & DiVincenzo, D. P. Coupled quantum dots as quantum gates. *Phys. Rev. B* **59**, 2070–2078 (1999).
[10] Jirovec, D. *et al.* A singlet-triplet hole spin qubit in planar ge. *Nat. Mater.* **20**, 1106–1112 (2021).
[11] Bravyi, S., Divincenzo, D. P. & Loss, D. Schrieffer-Wolff transformation for quantum many-body systems. *Annals of Physics* **326**, 2793 (2011).
[12] Chirolli, L. & Burkard, G. Decoherence in solid-state qubits. *Advances in Physics* **57**, 225–285 (2008).
[13] Lawrie, W. I. L. *et al.* Simultaneous single-qubit driving of semiconductor spin qubits at the fault-tolerant threshold. *Nature Communications* **14**, 3617 (2023).
[14] Hendrickx, N. W. *et al.* Sweet-spot operation of a germanium hole spin qubit with highly anisotropic noise sensitivity. *arXiv:2305.13150* (2023).